Materials Chemistry and Physics 343 (2025) 131009

Contents lists available at ScienceDirect

Materials Chemistry and Physics

journal homepage: www.elsevier.com/locate/matchemphys

Nanoscale engineering of Sr-doped ZnO nanorods/CuO nanocomposites for the photocatalytic treatment of methylene blue pollutant

Ali Tekin [a], Raşit Aydın [a,*], Ümmühan Akın [a], Osman Kahveci [b], Abdullah Akkaya [c], Hüsnü Kara [d], Bünyamin Şahin [d,e]

[a] Department of Physics, Faculty of Sciences, Selcuk University, Konya, Turkey
[b] Department of Physics, Faculty of Sciences, Erciyes University, Kayseri, Turkey
[c] Mucur Technical Vocational Schools, Tech. Prog. Department, Kırşehir Ahi Evran University, Kırşehir, Turkey
[d] Department of Basic Sciences, Faculty of Engineering, Necmettin Erbakan University, Konya, Turkey
[e] Department of Electrical and Computer Engineering, North Carolina State University, Raleigh, NC, USA

HIGHLIGHTS

- Sr-doped ZnO NRs/CuO composite films were synthesized by SILAR method.
- With Sr doping, the band gap energy value increased from 2.41 eV to 3.61 eV.
- Electrical measurements showed a decrease in the total resistivity values as the Sr doping ratio increased.
- The degradation results showed that 2.0 % Sr doping enhanced the photocatalytic degradation of ZnO NRs/CuO NC films.

ARTICLE INFO

Keywords:
ZnO nanorods/CuO
Strontium
TLM method
Bandgap
Photocatalytic degradation

ABSTRACT

This study investigates the effect of Sr doping on the physical and photocatalytic properties of ZnO nanorods/CuO nanocomposites. Various techniques were applied to understand how Sr doping modifies these films. SEM analysis showed that ZnO and CuO formed structures such as nanorods or nanowires. Sr-doped samples exhibited increased aggregation compared to undoped composites, with Sr doping levels of 2.0 % and 4.0 % leading to more pronounced morphological changes. AFM measurements showed an increase in average roughness from 70.53 nm to 111.83 nm with higher Sr doping levels. XRD analysis showed that the crystallite sizes decreased from 36.20 nm for undoped samples to 31.55 nm and 29.90 nm with 2.0 % and 4.0 % Sr doping, respectively. FTIR Spectroscopy provided insights into the chemical bonding changes induced by Sr doping. The bandgap analysis revealed that Sr doping in the ZnO/CuO nanocomposites enhanced the bandgap energy, with the value increasing from 2.41 eV in the undoped sample to 3.61 eV at 4.0 % Sr doping. Electrical conductivity measurements showed a decrease in total resistance values as the Sr doping ratio increased. The contact resistance values increased from 3.13×10^9 Ω in the un-doped samples to 3.22×10^8 Ω in the 4.0 % Sr-doped films. It was observed that 2.0 % Sr doping increased the photocatalytic degradation of the ZnO nanorods/CuO nanocomposite films, whereas 4.0 % Sr doping decreased this effect. Thus, the dynamic evaluation of the catalytic performance with TOF yields values of 0.176 and 0.184 for ZnO nanorods/CuO nanocomposites films and ZnO nanorods/CuO:Sr (2.0 %), respectively.

1. Introduction

Nanocomposites (NCs) are defined as materials formed by the combination of two or more different phases of nanometer size, and these materials are of great importance in terms of technological applications as well as disciplines such as materials science, physics, and chemistry. NCs containing metal oxides (MOs) are particularly interesting due to their superior physical, chemical, and optoelectronic properties. These materials combine the properties of individual MOs and new properties emerging at the nanoscale, making them extremely attractive for

* Corresponding author.
E-mail address: raydin@selcuk.edu.tr (R. Aydın).

https://doi.org/10.1016/j.matchemphys.2025.131009
Received 29 January 2025; Received in revised form 15 April 2025; Accepted 9 May 2025
Available online 14 May 2025

applications in catalysis, sensing, energy storage, and optoelectronics [1–4].

Metal oxide NCs provide significant benefits such as superior mechanical strength, improved electrical and thermal conductivity, and enhanced chemical stability by exploiting the harmonious interactions between various oxide materials. This compatibility results from the interfaces between the oxide phases where charge transfer, electron-hole separation, and enhanced catalytic activity occur. Furthermore, these nanomaterials' large surface area/volume ratio significantly enhances their reactivity and performance in applications such as photocatalysis and gas sensing [5–8].

Zinc oxide (ZnO) and copper oxide (CuO) have significant potential in the development of nanocomposites owing to their complementary properties among MO. ZnO is an n-type semiconductor with a wide band gap (~3.37 eV) and has unique properties such as high electron mobility, strong UV-light absorption, and high thermal stability. The hexagonal wurtzite crystal structure provides a robust and efficient structure, which is especially suitable for various technological applications such as optoelectronics, piezoelectric devices, and photocatalysis [9–12]. In contrast, CuO is a p-type semiconductor with a relatively narrow band gap (~1.2 eV), allowing it to absorb visible light efficiently. The CuO compounds have attracted great interest due to their high electrical conductivity, superior photothermal properties, and effective catalytic performance. The combination of its monoclinic crystal structure and its ability to function as an efficient p-type semiconductor makes CuO an ideal candidate for the formation of composites with ZnO [13–15].

The combination of ZnO nanorods (NRs) and CuO in a nanocomposite structure produces ZnO NRs/CuO NC that exhibit tunable properties that exceed those of the individual oxides. The synthesis of ZnO NRs/CuO NC reduces recombination by increasing electron-hole separation, thereby increasing the efficiency of the material for photocatalysis and sensing. Furthermore, the structural flexibility of these NCs allows the optimization of the surface area, morphology, and phase composition, making them highly adaptable for specific applications. ZnO NR/CuO NCs have shown remarkable potential in a wide range of applications. The potential of these materials as effective photocatalysts in water splitting and environmental remediation has been extensively studied. Furthermore, NC has remarkable efficacy in medical applications such as gas sensing, energy storage devices, and even antimicrobial agents [16–19].

Doping of ZnO/CuO nanocomposite films is a widely used effective method for improving structural, optical, electrical, and photocatalytic properties. The addition of doping elements facilitates the separation of charge carriers by changing the band structure and increasing reactive oxygen species formation during photocatalysis. For example, transition metals such as Mn, Fe, Al, and Cu doped into ZnO/CuO composites increase visible light absorption and decrease recombination rates of electron-hole pairs. Therefore, the doping process plays a critical role in optimizing the performance of ZnO/CuO films in photocatalytic and other functional applications [20–22].

Strontium (Sr) was chosen as a doping element due to its unique combination of physical and chemical properties, which are particularly suitable for modifying the structural and electronic properties of ZnO/CuO nanocomposite films. Sr has a larger ionic radius (1.18 Å) than the Zn^{2+} ion (0.74 Å), enabling it to fit into the ZnO lattice efficiently, generating lattice stress and introducing structural defects such as oxygen vacancies. Such defects are known to enhance the separation of charge carriers and increase the surface reactivity, which is highly beneficial for photocatalytic activity. Furthermore, Sr is an alkaline earth metal with a valence of +2, so the charge balance is maintained when replacing the Zn^{2+} ion. Sr is less toxic and environmentally safer than other dopants, such as rare earth elements or transition metals [23,24].

Researchers have frequently studied the synthesis of ZnO NRs/CuO NCs. Various techniques such as hydrothermal method, sol-gel method, co-precipitation methods, thermal oxidation methods, electrochemical deposition, microwave-assisted synthesis, chemical vapor deposition (CVD), and successive ionic layer adsorption and reaction (SILAR) have been developed to optimize properties for specific applications [25–28]. Among these methods, the SILAR technique is a versatile and cost-effective method widely used in the synthesis of thin films and nanostructures of MO, including ZnO NRs/CuO NCs. This technique is widely used because of its ease of application, the possibility of precise control over film thickness, and the ability to be compatible with various substrates [29,30].

Although conventional wastewater treatment methods effectively remove solid wastes and certain chemical pollutants, they are often ineffective in degrading persistent organic pollutants, such as dyes, pharmaceuticals, and pesticides. In this context, semiconductor-based photocatalysis is a promising approach for environmental remediation, offering a sustainable and efficient method for degrading a wide range of organic compounds under light irradiation. Removing organic pollutants in this way significantly benefits the ecosystem and human health [31–34].

ZnO NRs/CuO nanocomposite materials are being studied to solve the problem of environmental pollution through photocatalytic degradation. The ability of these composites to work effectively at different light wavelengths, coupled with enhanced charge separation, provides high efficiency for the degradation of organic pollutants [35–37]. Recent studies in the literature have also shown that ZnO NRs/CuO NCs exhibit superior photocatalytic performance to those of their constituent components. For example, Kumari et al. investigated the high performance of ZnO NRs/CuO NC in degrading organic dyes such as methylene blue, rhodamine B, and methyl orange under both UV and visible light [38]. In another study, Xu et al. found that ZnO NRs/CuO NC synthesized by hydrothermal method showed improved photocatalytic activity for the degradation of methylene blue (MB) dye under visible light [39].

So far as we know, no study has examined the influence of strontium (Sr) doping on the main characteristics and photocatalytic efficacy of ZnO NRs/CuO NC was investigated by the degradation of methylene blue dye under UV light. Accordingly, this study aimed to fabricate Sr-doped and undoped ZnO NR/CuO composites using the SILAR method and to investigate the effect of Sr doping on their structural, morphological, electrical, and photocatalytic properties. The remainder of this paper is structured as follows: Part 2 describes the synthesis and characterization details of undoped and Sr-doped ZnO/CuO nanocomposite films by SILAR method. Part 3 presents the results and discusses the films' structural, morphological, optical, electrical, and photocatalytic properties. Finally, Part 4 summarises the results obtained from the study and highlights the effect of Sr doping on the performance of the nanocomposite films.

2. Experimental section

Sr-doped ZnO NRs/CuO nanocomposite films were fabricated using the SILAR method, which allows the controlled deposition of ionic species on the substrate surface through adsorption and reaction steps. This method facilitates the sequential growth of oxide materials by precisely adjusting the stoichiometry and film thickness. The precursor salts used in the synthesis of the films are zinc acetate dihydrate [$C_4H_6O_4Zn{\cdot}2H_20$, Merck KGaA], copper (II) chloride dihydrate [$Cl_2Cu{\cdot}2H_2O$, Merck KGaA], and strontium chloride hexahydrate [$Cl_2Sr{\cdot}6H_2O$, Merck KGaA]. Analytical grade reagents were used, and deionized water was used as the solvent to maintain purity throughout the process. The glass substrates were cleaned by sequential washing with acetone and deionized water. This process ensured uniform adhesion of the deposited ions by removing surface contaminants. 100 mL of ZnO/CuO aqueous precursor solution was prepared using 0.1 M $C_4H_{10}O_6Zn$ solution (60 mL) and 0.1 M $Cl_2CuH_4O_2$ solution (40 mL). The solutions were thoroughly mixed to ensure homogeneity and complete salt dissolution. The cleaned substrates were immersed in a ZnO/CuO

solution at room temperature for 20 s to adsorb Zn^{2+} and Cu^{2+} ions on the substrate surface. Subsequently, the substrates were rinsed with deionized water for 20 s to remove loosely bound ions and prevent the formation of unwanted by-products. The adsorption and reaction steps above were repeated 10 times alternately to obtain the desired ZnO NRs/CuO nanocomposite structure. To investigate the contribution of Sr^{2+} to the properties of the ZnO NRs/CuO nanocomposite film, $SrCl_2{\cdot}6H_2O$ salt was added to the ZnO NRs/CuO solution, and Sr^{2+} ions were co-adsorbed on the surface. Sr-doped composite films were produced by applying the above SILAR procedure. After deposition, the samples were thermally annealed in a muffle furnace at 400 K for 45 min. This process improves the composite material's crystallinity and increases the nanocomposite's overall stability by providing firm adhesion between ZnO and CuO. The fabrication procedures of the SILAR have been schematically delineated in Fig. 1. The synthesized ZnO NRs/CuO NC were analyzed to determine their structural, morphological, electrical, and optical properties and photocatalytic performances using a range of characterization techniques.

X-ray diffraction (XRD; Bruker D8 Advance, CuKα, $\lambda = 1.518$ Å) was used to evaluate the crystallographic structure, while scanning electron microscopy (SEM; Zeiss evo Ls 10), atomic force microscopy (AFM; NT-MDT/Ntegra Solaris), and energy dispersive X-ray spectroscopy (EDX) were used for morphological and compositional analysis. The functional groups were identified using Fourier transform infrared (FTIR) spectrometry (Bruker Vertex70). The Jasco V-670 UV–Vis spectrophotometer was used to study the optical characteristics. The thicknesses of the composite films were determined with the AEP Technology NanoMap 500 LS 3D profilometer by averaging the thicknesses measured at different points of the films. Current-voltage (I–V) measurements were made using a Zive Sp1 (Wonatech) Potentiostat device for the electrical analysis. Au contact motifs were designed on thin-film samples according to the transfer-length method (TLM).

The photocatalytic performance of the synthesized ZnO NRs/CuO NC composites, including those doped with Sr at concentrations of 2.0 % and 4.0 %, was evaluated by monitoring the degradation of methylene blue (MB) under UV light exposure. An MB solution with a concentration of 10 ppm was prepared in distilled water, and its pH was adjusted using NaOH and the pH value of the final solution was 10. Subsequently, 30 mg of each catalyst sample was added to 30 mL of the dye solution and stirred for 20 min to achieve adsorption-desorption equilibrium. Each sample mixture was irradiated with UV light (3 Watt, 395–400 nm), with 3 mL aliquots collected at 10min intervals. The samples were centrifuged at 3000 rpm for 4 min to remove the photocatalysts, and absorbance measurements were performed at 665 nm using a Shimadzu UV-1201 spectrophotometer to assess MB degradation. Over 120 min of UV exposure, a marked reduction in dye color and absorbance was observed. Photocatalytic degradation measurements were conducted only once for each sample due to experimental constraints, and the absorbance values monitored at 665 nm exhibited a consistent decreasing trend without any observable anomalies, indicating reliable measurement stability throughout the irradiation period.

3. Results and discussion

3.1. Morphological analyses

SEM was used to analyze the surface structure and aggregation behavior of the synthesized NC. SEM images of un-doped and Sr-doped ZnO NRs/CuO NCs at 2.0 % and 4.0 % concentrations are shown in Fig. 2. From the un-doped ZnO NRs/CuO SEM images, both ZnO and CuO form structures such as nanorods or nanowires. ZnO NRs are typically hexagonal and longer, while CuO nanowires appear much shorter and dispersed. However, Sr^{2+} doping at 2.0 % concentration caused noticeable changes in the morphological characteristics. From the images, we observed that ZnO NRs became larger and more prominent, and CuO nanowires came together to form clusters. A denser and tighter surface structure was obtained at an Sr^{2+} doping concentration of 4.0 %. The morphological changes observed by Sr doping in ZnO/CuO nanocomposite films are mainly related to ionic radius mismatch, defect formation, and changes in surface energy. The changes in the surface structure of ZnO NRs/CuO NC upon Sr-doping can be attributed to several factors. Sr^{2+} ions have a larger ionic radius (1.21 Å) compared to Zn^{2+} (0.74 Å) and Cu^{2+} (0.73 Å).

When Sr^{2+} is added to the ZnO NRs/CuO lattice, the replacement of smaller ions by larger Sr^{2+} ions can lead to a change in the lattice and surface structures. That is, lattice stress and distortions may occur. The addition of Sr^{2+} ions can affect the nucleation and growth kinetics of ZnO and CuO crystals. During the synthesis process, Sr^{2+} ions may interact differently with ZnO and CuO compared to the un-doped composites. These interactions can change the diffusion rates of Zn^{2+} and Cu^{2+} ions and thus affect the crystallization process. This can lead to changes in surface morphology. Furthermore, Sr doping can affect the preferential growth orientation of ZnO nanostructures by changing the surface energy of certain crystal planes. Such orientation changes can directly affect the growth shape of grains and nanostructures, resulting in morphological differences [23,40–42].

EDX was used to determine the elemental composition of the ZnO NRs/CuO NC and confirm the successful doping of the Sr^{2+} dopant.

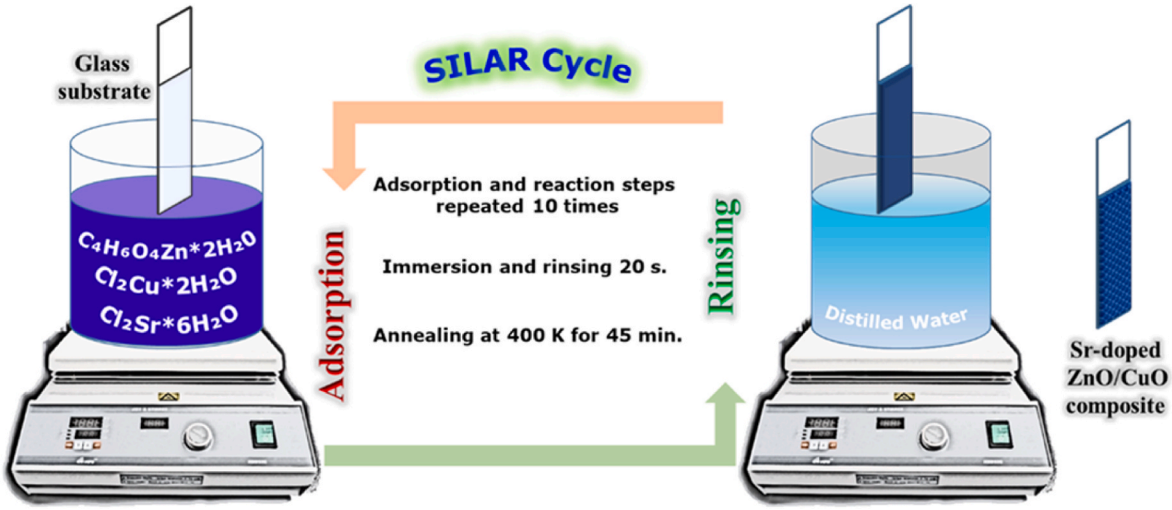

Fig. 1. Demonstration of the fabrication of Sr-doped ZnO/CuO nanocomposite films by SILAR procedure.

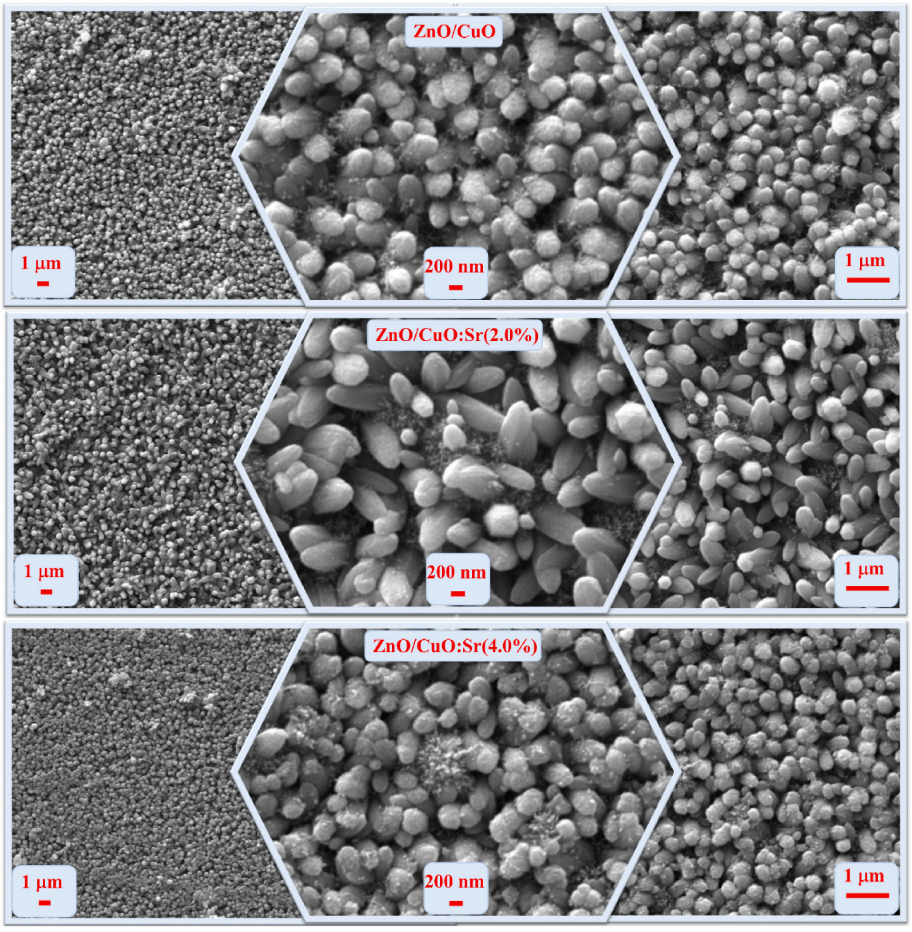

Fig. 2. SEM micrographs of ZnO NRs/CuO NCs with various Sr doping concentrations (0.0 %, 2.0 %, and 4.0 %). Both ZnO and CuO can form one-dimensional structures like nanorods or nanowires.

Fig. 3 shows the EDX spectra of the ZnO NRs/CuO and ZnO NRs/CuO: Sr (4.0 %) composite films. EDX mapping confirmed the successful incorporation of Sr^{2+} into the ZnO NRs/CuO matrix and its uniform distribution along the sample surface. The atomic percentages of Zn, Cu, O, and Sr in various regions of the composite are presented in Fig. 3. In the EDX elemental mapping; specific colors were assigned to each element to visually represent their distribution in the composite material: Zn, yellow; Cu, blue; O, green; and Sr, red.

Atomic Force Microscopy (AFM) was used to investigate the surface topography and roughness of the Sr-doped ZnO NRs/CuO NC. Fig. 4 shows 2D and 3D AFM images of un-doped and Sr-doped ZnO NR/CuO nanocomposite structures. AFM images of the un-doped samples showed that the ZnO NRs/CuO composite has a relatively smooth surface structure with uniformly distributed nanoscale grains, consistent with its polycrystalline nature. The root mean square (Sq) roughness was approximately 91.42 nm, and the average roughness (Sa) was 70.53 nm. The entropy value, which measures the degree of surface complexity, was found to be 11.80, reflecting a relatively regular topography with minimal surface irregularity. After 2.0 % Sr doping, significant changes were observed in all three parameters. Sa increased to 96.33 nm, and Sq increased to 127.56 nm. This indicates that Sr^{2+} doping contributes to forming larger or more protruding grains. The entropy value for the 2.0 % Sr-doped composite also increased to 12.23, suggesting a more complex and less homogeneous surface morphology. When the Sr dopant rate was 4.0 %, the Sa value increased to 111.83 nm, and the Sq value increased to 143.82 nm, indicating a significant increase in the surface roughness of the composites. The entropy also increased to 12.43, indicating the composite's increasing surface complexity and irregularity. These values are also presented in Table 1. The increase in Sa, Sq, and entropy values due to increasing Sr content can be attributed to the lattice distortion caused by size mismatch when Sr is incorporated into the ZnO NR/CuO lattice, changing the nucleation and growth dynamics of ZnO and CuO crystallites. Moreover, doping can cause changes in the surface energy of ZnO NRs/CuO composites and in the electrostatic interactions between Sr^{2+} ions and particles [43–48].

3.2. Xray diffraction analysis

XRD was used to analyze the crystal structure and phase composition of undoped and Sr-doped ZnO NRs/CuO NC. The XRD diffraction patterns obtained depending on the Sr content are given in Fig. 5. The XRD spectrum of the undoped ZnO NR/CuO composite shows characteristic peaks corresponding to the wurtzite structure of ZnO (JCPDS No. 01-076-0704) and the monoclinic phase of CuO (JCPDS No. 00-080-1917) [49,50]. Notable diffraction peaks were observed at $2\theta \approx 31.97°$, 34.63°, 36.45°, 47.72°, 56.75°, 63.02°, 66.51°, 68.09°, 69.22°, 72.71° and 77.08°, associated with the (100), (002), (101), (102), (110), (103), (200), (112), (201), (004) and (202) planes of ZnO, as well as peaks at $2\theta \approx 35.70°$, 38.96°, 48.68°, 58.11°, 61.76°, 72.71° and 75.11°, corresponding to the ($\bar{1}$**11**), (111), (**20**$\bar{2}$), (202), ($\bar{1}$**13**), (311) and (004) planes of CuO. After doping with 2.0 % and 4.0 % Sr^{2+}, slight shifts toward lower 2θ angles were observed, especially in the diffraction peaks of ZnO, indicating that Sr ions were successfully doped into the ZnO lattice. In addition, the diffraction peaks in Fig. 5 show that the intensity of the ZnO peaks changes with doping. This shift and change in the peaks was probably due to the displacement of the smaller Zn^{2+} ions

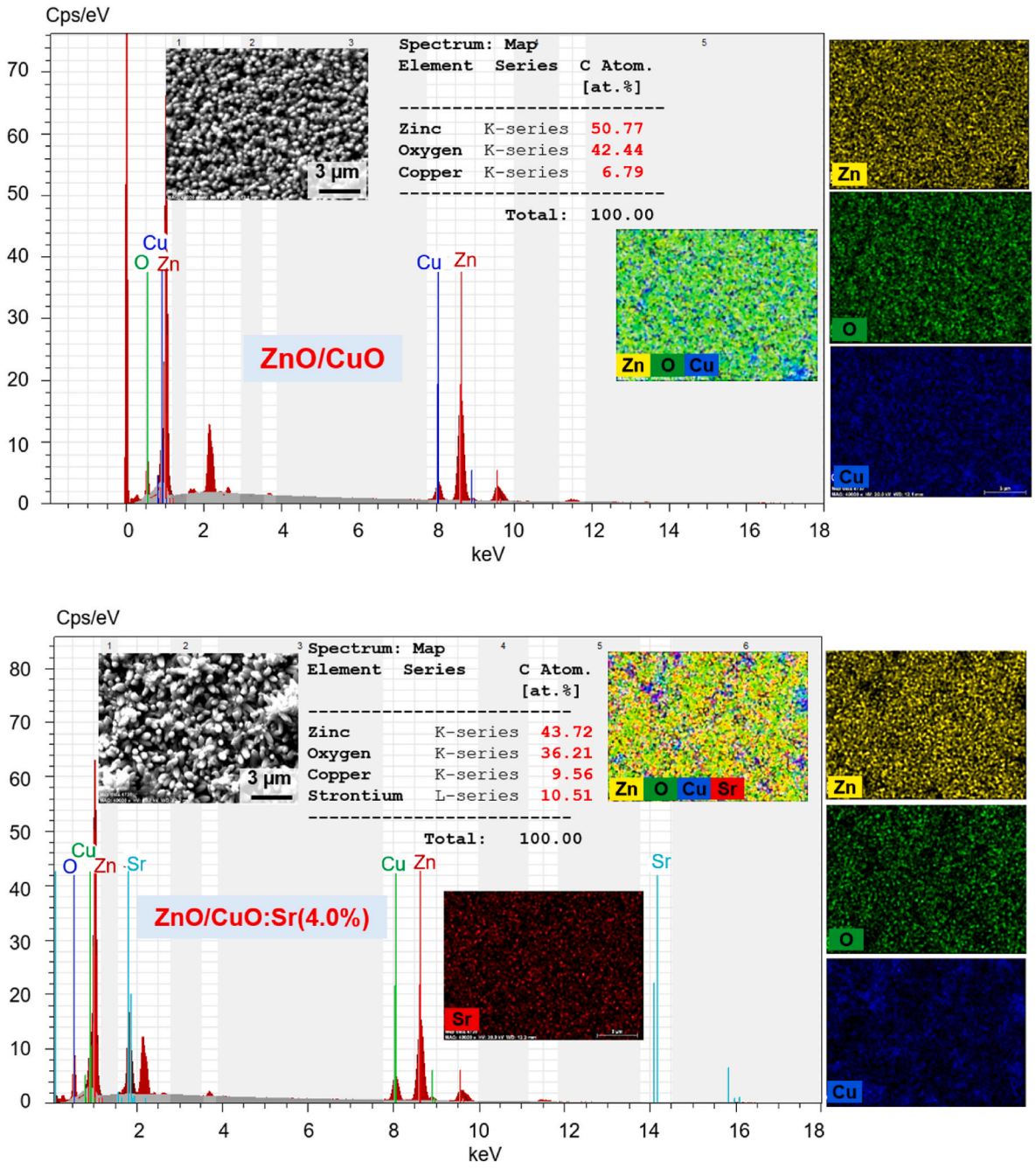

Fig. 3. EDX spectra and elemental mapping of Sr-doped ZnO NRs/CuO NCs. The EDX mapping shows that Sr is present in the ZnO NRs/CuO matrix and is evenly distributed on the sample surface.

by the larger Sr^{2+} ions, leading to strain in the crystal lattice. The CuO peaks remained largely unaffected by Sr doping, indicating that Sr doping primarily affects the ZnO lattice [51–53].

The mean value of the crystallite size (D) was determined using the well-known Scherrer equation [54].

$$D = \frac{k\lambda}{\beta \cos\theta} \quad (1)$$

where k is the shape factor, λ is the X-ray wavelength, β is the full width at half maximum θ is the diffraction angle. All ZnO and CuO diffraction peaks were considered when finding the average D values. The average crystallite sizes were calculated as 36.20 nm for undoped samples, 31.55 nm for 2.0 % Sr-doped composites, and 29.90 nm for 4.0 % Sr-doped composites. The reduction in crystallite size with increasing Sr^{2+} content implies that Sr^{2+} doping disrupts the growth of larger, well-ordered crystallites, leading to smaller, more strained particles. The size difference between Zn^{2+} (0.74 Å) and Sr^{2+} (1.21 Å) ions leads to the formation of intrinsic stress in the ZnO lattice by Sr doping. This stress may be the reason for the decrease in crystallite size. In addition, Sr ions inhibit the growth of crystals by reducing mobility at grain boundaries. This mechanism explains the regular reduction of the crystallite size despite increasing doping. The changes in peak intensities and decrease in crystallite size with increasing Sr^{2+} concentration may be primarily due to lattice distortion, strain, and defects introduced by the larger Sr^{2+} ions, which disrupt the crystal structure of ZnO. Sr doping affects the nucleation and growth processes, leading to smaller crystallites and a more irregular lattice, changing the XRD peak intensities [55–57].

Sr doping leads to a decrease in crystallite size (XRD) but also to

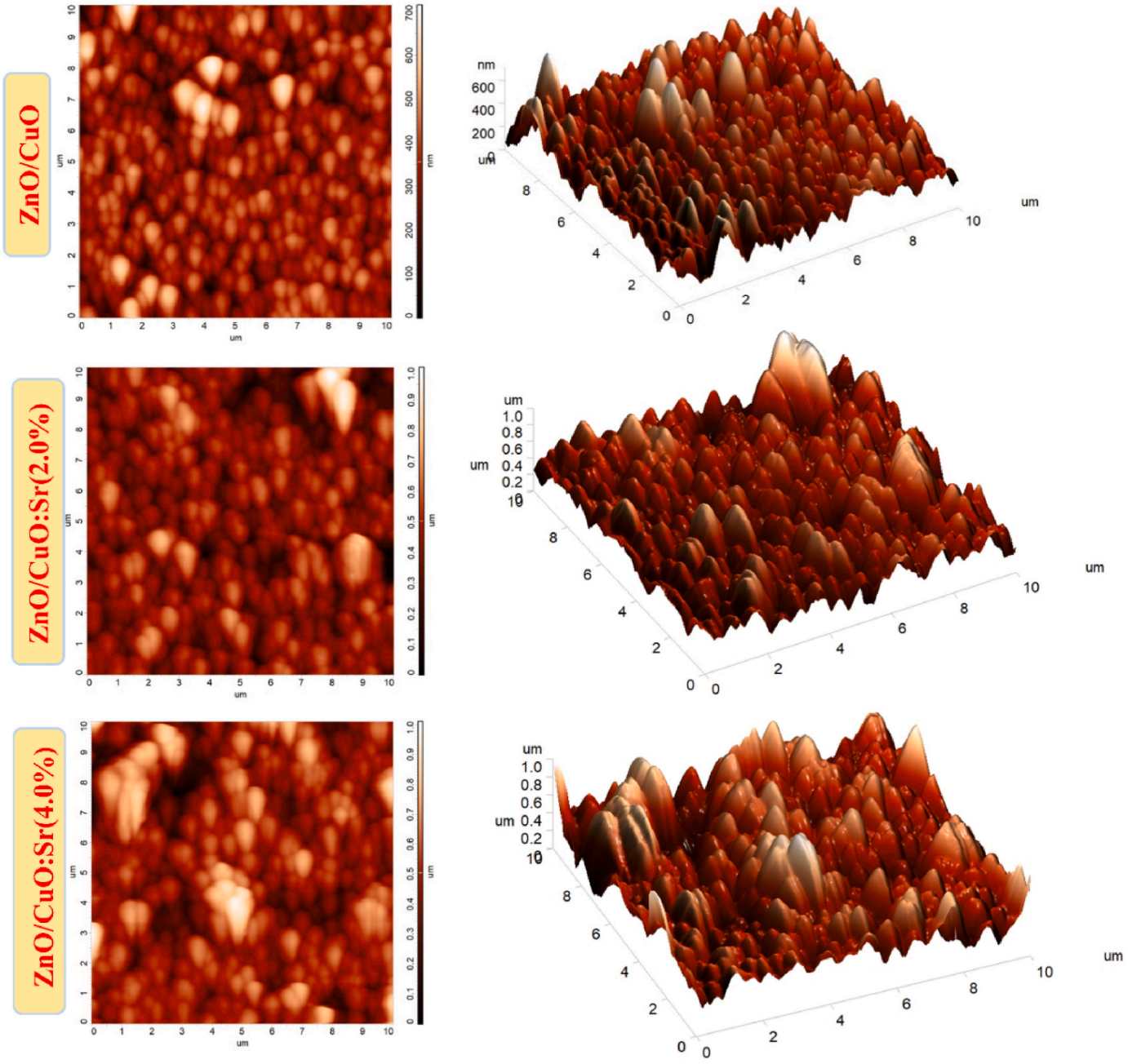

Fig. 4. AFM topographic images of ZnO NRs/CuO NCs with different Sr doping levels. The variations in surface roughness among the samples indicate that Sr doping significantly alters the nanometer-scale morphology of the ZnO–NRs/CuO composites.

Table 1
Average roughness (Sa), root mean square (Sq), entropy, optical bandgap energy, and crystallite size values of ZnO NRs/CuO NC films as a function of Sr concentration in the growth solutions of the SILAR process.

Sample Name	Average Roughness Sa (nm)	Root Mean Square Sq (nm)	Entropy	Optical Bandgap (eV)	Crystallite Size (nm)
ZnO NRs/ CuO	70.53	91.42	11.80	2.41	36.20
ZnO NRs/ CuO:Sr (2.0 %)	96.33	127.56	12.23	3.42	31.55
ZnO NRs/ CuO:Sr (4.0 %)	111.83	143.82	12.43	3.61	29.90

larger clusters on the surface (SEM) and higher surface roughness (AFM). These techniques complement the multiscale effects of Sr doping on the nanocomposite, and the differences between them are due to their methodological characteristics. The AFM results agree with these findings, showing increased surface roughness (higher Sa and Sq values) with Sr doping. The SEM images also support the XRD observations by revealing changes in particle morphology.

3.3. FTIR analyses

Fourier Transform Infrared (FTIR) spectroscopy was performed to investigate the chemical bonding and vibrational characteristics of the Sr-doped ZnO NRs/CuO NC. FTIR spectra were recorded for the undoped, 2.0 % Sr-doped, and 4.0 % Sr-doped samples, covering the spectral range from 400 to 4000 cm^{-1} (Fig. 6).

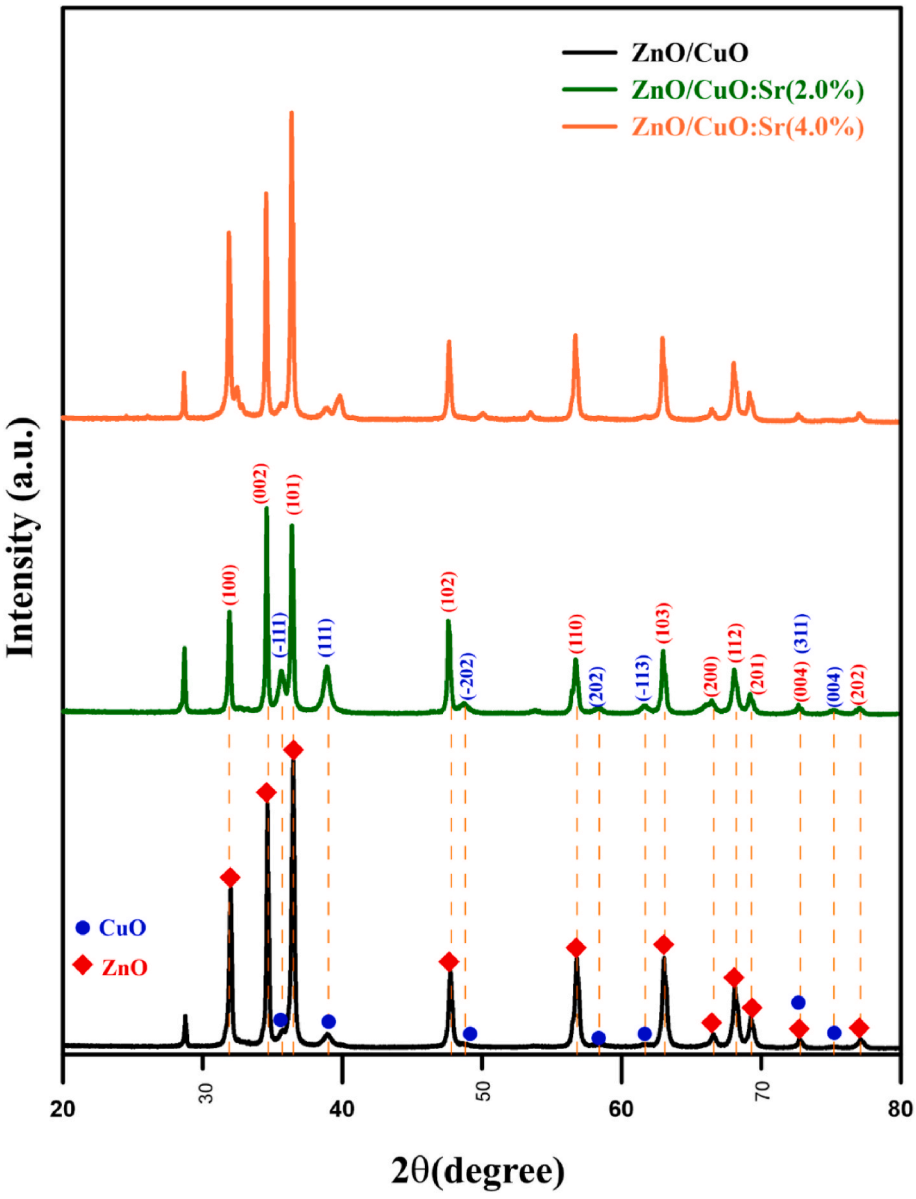

Fig. 5. XRD patterns of ZnO/CuO NCs doped with Sr. The XRD pattern of the undoped ZnO/CuO composite exhibited well-defined peaks characteristic of the wurtzite structure of ZnO and the monoclinic phase of CuO.

The stretching modes of metal-oxygen (M-O) bonds in metal-oxide materials typically occur in the low-frequency region (fingerprint region) of the FTIR spectrum, generally below 1000 cm^{-1}. So, peaks, appearing at ~447 to ~888 cm^{-1}, can be assigned to the metal-oxygen (M − O) (M = Zn, Cu) stretching modes that arise from inter-atomic vibrations [58,59]. Also, the absorption peak located at 880 cm^{-1} was appointed to the characteristic stretching mode of the Zn–O bonds [59, 60]. A broad absorption band diverse regions of the FTIR spectrum (located near 3440 cm^{-1}) can be assigned to O–H stretching vibrations of the hydroxyl groups, signifies to O–H stretching modes of surface adsorbed water molecules or hydroxyl groups in M − OH (M = Zn, Cu) and indicates that presence of adsorbed water molecules on the ZnO NRs/CuO NCs films [59,61].

Also, peaks between 2356 cm^{-1} and 2922 cm^{-1} can be attributed to C═O and $–CH_2$ vibrations from the residual precursors and organic contaminations. The weaker band at 1647 cm^{-1} was identified as the H–*O*–H bending mode. Stretching vibrations of ═ located at 1740 cm^{-1}, the band near 1375 cm^{-1} is associated with C–O stretching vibrations, and bending and wagging bands of C–H are observed in the range 1451 and 1316 cm^{-1}. And finally, peaks at 1235-1035 cm^{-1} are attributed to characteristic C–O–C and C–O–H bending and stretching vibrations [59, 61]. The FTIR results are thus consistent with those obtained by XRD and EDX [62–66].

3.4. Optical analyses

The band structures of semiconductor materials used in electronic and optoelectronic devices, which have an important place in today's technology world, are critical for determining their electrical and optical properties. The semiconductor materials have two basic types of band structures: direct and/or indirect. The most commonly used method to determine whether the band gap is direct or indirect is to plot the graphs of $(\alpha h\upsilon)$ versus photon energy for certain power values. Therefore, whether the Tauc graphs drawn for power values exhibit a steep/linear increase is checked. In the UV–Vis measurements conducted, the absorption edge of the ZnO/CuO films exhibited a sharp and well-defined increase in absorbance, which is indicative of direct electronic transitions. The ZnO NRs/CuO material used in the present study was

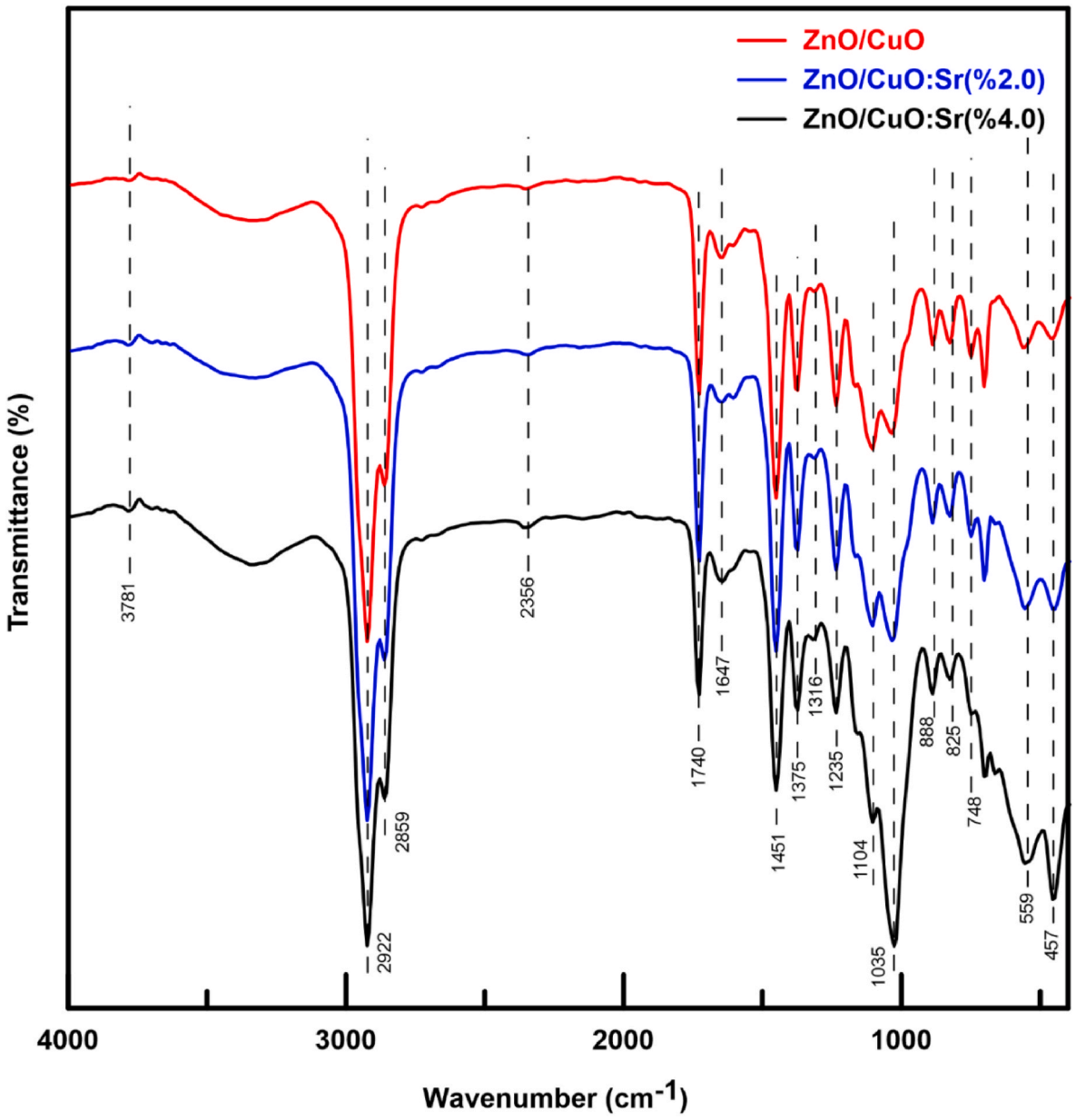

Fig. 6. FTIR spectra of Sr-doped ZnO NRs/CuO NCs. The FTIR analysis confirmed that Sr doping induces significant modifications in the vibrational characteristics of ZnO NRs/CuO NCs.

observed to have a direct bandgap, and the bandgap values were determined using the Tauc model [67]:

$$(\alpha h\upsilon) = A\left(h\upsilon - E_g\right)^m \quad (2)$$

In the expression above, $h\upsilon$ is the photon energy, α is the absorption coefficient, E_g is the band gap energy, and A parameter is known as the energy-independent Tauc constant. The other parameter, m, is a constant corresponding to 1/2 for direct transition and 2 for indirect transition. The direct nature of the transition is further supported by the linearity of the Tauc plot using the $(\alpha h\upsilon)^2$ vs. $h\upsilon$ form. As shown in Fig. 7, the direct bandgap values of ZnO NRs/CuO films prepared using different Sr doping concentrations were obtained from the graphs of $(\alpha h\upsilon)^2$ against $h\upsilon$ and by extrapolating the graphs to the zero-absorption value of the linear region.

For the un-doped ZnO NRs/CuO composite, the bandgap was found to be approximately 2.41 eV, which is typical for a combination of ZnO (with a wider bandgap around 3.3 eV) and CuO (with a narrower bandgap around 1.7 eV). This value reflects the composite nature, where the interaction between the ZnO and CuO phases leads to band alignment and intermediate electronic states. When doped with 2.0 % or 4.0 % Sr, the band gap broadened from 3.42 to 3.61 eV. These changes in the bandgap values can be attributed to the formation of different crystal structures with different doping ratios or to the inhomogeneities observed in the film. The increase in bandgap observed with Sr doping in ZnO NRs/CuO NCs can be explained by multiple interrelated factors, including the reduction in defect states, lattice distortion, and modification of the electronic band structure.

Additionally, it can be shown that the calculated E_g values agree with similar studies in the literature, considering the structural differences [43,68–71].

Fig. 8 shows the transmittance curves of un-doped, 2.0 % Sr, and 4.0 % Sr doped ZnO/CuO nanocomposite films in the 190–3500 nm wavelength range. The lowest transmittance (~20–50 %) in all spectral regions, especially high absorption in the UV and visible region, was observed in the un-doped film. In the 2.0 % Sr-doped film, the

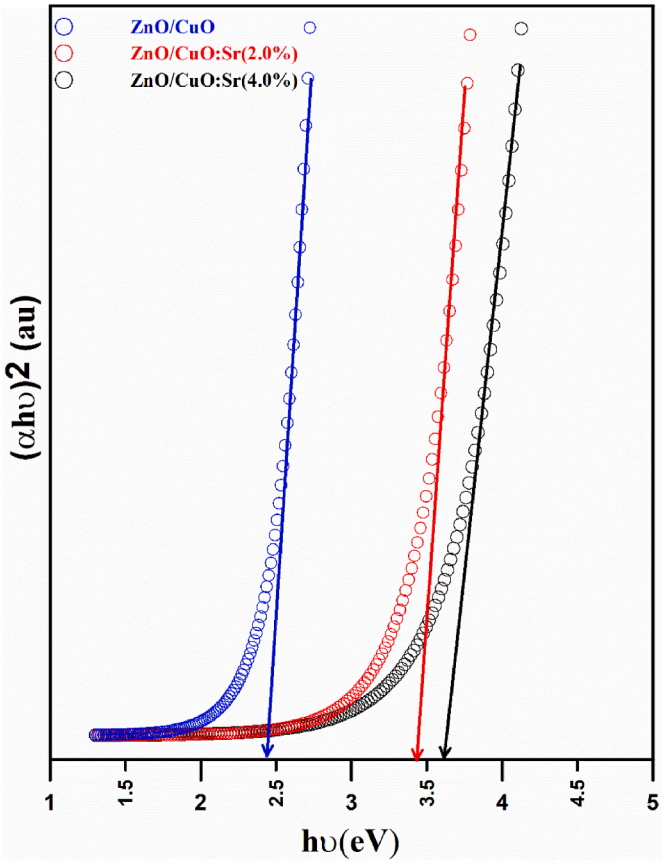

Fig. 7. Tauc plot analysis for determining the optical bandgap of ZnO NRs/CuO NCs with various Sr doping. Bandgap analysis revealed that Sr doping in ZnO NRs/CuO NCs effectively increased the bandgap energy.

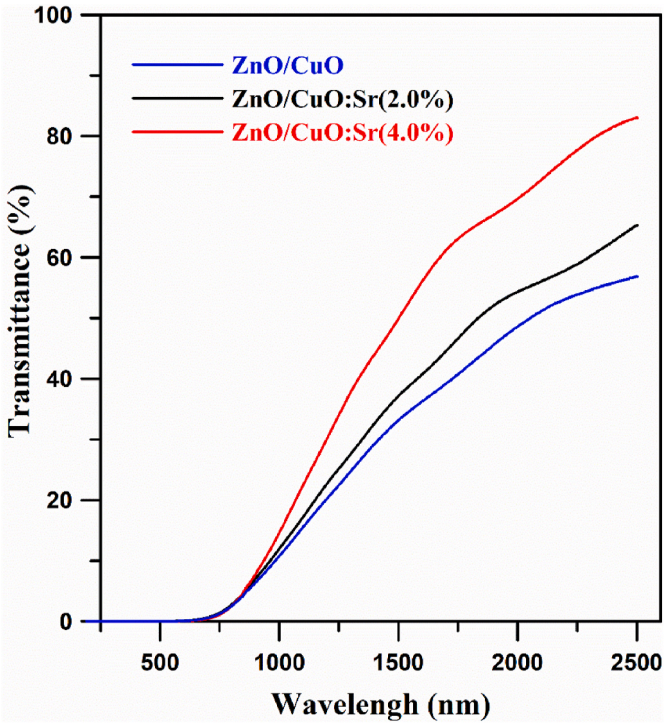

Fig. 8. Optical transmittance curves of undoped, 2.0 % Sr and 4.0 % Sr doped ZnO/CuO nanocomposite films. Optical transmittance increases with increasing Sr doping.

transmittance curve is generally higher, especially between 400 and 1000 nm, showing a significant increase (~50–70 %). When the Sr contribution is 4.0 %, the transmittance increases further and reaches values between ~70 and 85 % in the NIR region. Sr^{2+} doping stretches the crystal structure by replacing Zn^{2+} ions in the ZnO lattice. Accordingly, widening the band gap may lead to an increase in transmittance. Sr doping increases crystallinity, and absorption centers such as oxygen vacancies in the ZnO/CuO system are reduced (reduction of defect levels). This increases the transmittance ratio. The increase in transmittance can also be attributed to the film thickness. The thicknesses of un-doped, 2.0 % Sr-doped and 4.0 % Sr-doped ZnO/CuO composite films were found to be 466 nm, 405 nm, and 292 nm, respectively. As the Sr doping increases, the thickness of the films decreases, and the films become more transparent, increasing optical transmittance [72–74].

3.5. Electrical analysis

The electrical properties of doped and un-doped ZnO NR/CuO NC thin films were analyzed using the Transfer Length Method (TLM) [75]. The electrical properties of materials are important for understanding current conduction mechanisms. Moreover, the electrical properties are important for understanding photocatalytic conversion. Because of the surface morphology, the presence of doped atoms and the defects caused by doping can affect the conductivity properties of thin-film materials. Similarly, the defects caused by doping and the presence of surface states affect the photocatalytic behavior by changing the positions of the band edges. For example, differences in the doping and metal oxide structure ratios cause changes in the donor concentrations and changes in the photocatalytic activity [76], and donor impurities significantly affect the electrical conductivity [77]. The TLM method was preferred for the electrical analysis of ZnO NR/CuO NC thin film samples, which also considers properties such as contact resistance, effective transfer length, and crowding of the current. In this method, the formulas used to calculate the electrical properties of thin-film materials are as in Equation (3) and Equation (4) below.

$$R_c = \frac{R_{sk} L_T}{w} \coth\left(d/L_T\right) \tag{3}$$

$$L_T = \sqrt{\frac{\rho_c}{R_{sk}}} \tag{4}$$

In these equations, R_c represents the total contact resistance, R_{sk} represents the modified sheet resistance, L_T represents the effective transfer length, and ρ_c represents the specific contact resistance. This method has four contacts of width w and length d with different distances between them. Gold (Au) contact patterns were produced on the surfaces of un-doped ZnO NRs/CuO NC, 2.0 % and 4.0 % Sr-doped ZnO NRs/CuO NC thin films under high vacuum by thermal evaporation (~50 nm thickness) with a shadow mask. The parameters of the contacts are given in Fig. 9(a), which includes a schematic drawing of the contacts. Current-voltage (I–V) measurements were taken with a Zive Sp1 Potentiostat device ranging from −5 to +5 V at a scanning rate of 50 mV/s. The data were exported using software integrated with the device [78], and the parameters were calculated using VEE Pro-based SeCLaS software [79]. I–V characteristics were obtained for all thin film samples over two contacts (@1–2, @2–3, @3–4) with different d distances (d_1, d_2, d_3). Fig. 9(b) shows the I–V characteristics obtained from contacts 2 and 3 (@2–3) for doped and un-doped ZNO NRs/CuO NC films. R_1, R_2, and R_3 series resistance values corresponding to the d_1, d_2, and d_3 contact distances were obtained for each thin film. More detailed information on obtaining these resistance values from I–V characteristics was reported in the studies of Soğan, S. et al. [80].

The calculated electrical parameters are summarized in Table 2. When the distance between the contacts increased, the resistance values increased for all samples. This is expected because the distance that

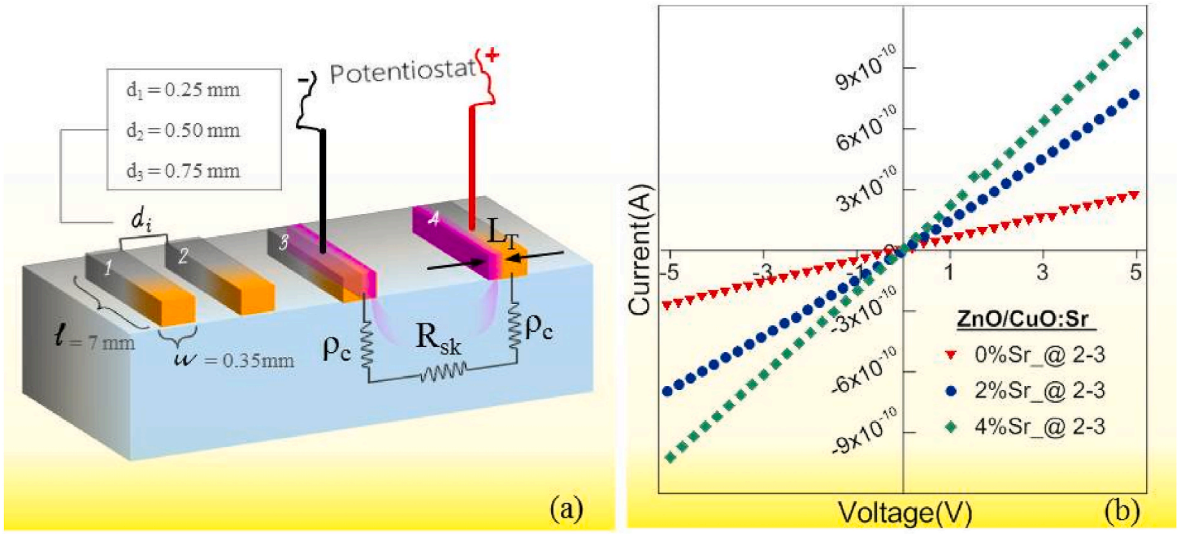

Fig. 9. (a) Schematic drawing of the contacts designed for the TLM method and some embedded parameters; (b) I–V characteristics obtained from contacts 2 and 3 for thin films.

Table 2
Electrical parameters of ZnO NRs/CuO NC and Sr-doped ZnO NRs/CuO NC thin films from TLM method.

Electrical Parameters	ZnO NRs/CuO	ZnO NRs/CuO: (2.0 %Sr)	ZnO NRs/CuO: (4.0 %Sr)
R_1 (Ω)	1.13×10^{10}	6.02×10^{9}	2.08×10^{9}
R_2 (Ω)	1.82×10^{10}	6.34×10^{9}	4.58×10^{9}
R_3 (Ω)	2.22×10^{10}	6.58×10^{9}	7.42×10^{9}
R_c (Ω)	3.13×10^{9}	2.87×10^{9}	3.22×10^{8}
ρ_c (Ω.cm^2)	1.57×10^{7}	2.53×10^{7}	0.34×10^{7}
L_T (μm)	1.43	25.33	3.01

charge carriers will travel for current conduction increases. At the same time, this observed correlation may also indicate that the thin film is homogeneously and uniformly distributed on the surface [81]. Because the thickness differences within the thin films could disrupt the correlation that changes with distance. It can be observed from Table 2 that the effective transfer length values differ for thin films. On the other hand, the series resistance values decreased with the effect of doping. It can be seen that Sr doping affects the change in total contact resistance (R_c). While the R_c value is 3.13×10^9 Ω for the ZnO NRs/CuO thin film sample, it decreases to 2.87×10^9 Ω for 2.0 % Sr-doped ZnO NRs/CuO: (2.0 % Sr) and further decreases to 3.22×10^8 Ω for ZnO NRs/CuO: (4.0 % Sr) when 4.0 % Sr was doped. The results show that Sr^{2+} doping increases conductivity.

This result may be related to the increase in the grain size observed in the SEM and AFM results. Similarly, in the studies of Vijayan, T. A. et al. [82], Sr doping was attributed to the larger grain size and the increase in conductivity. The ρ_c is 1.57×10^7 Ω cm^2 for undoped ZnO/CuO, increases to 2.53×10^7 Ω cm^2 with 2.0 % Sr doping, but decreases to 0.34×10^7 Ω cm^2 with 4.0 % Sr doping. This electrical parameter, which is determined specifically for the film, may also be related to photocatalytic performance because the increase in current carrier concentration reduces the catalytic performance [76] and the electrical resistance value [83]. The results show that the electrical parameters are affected by both the doping and the structural and morphological changes of the different metal oxide composites.

3.6. Photocatalytic degradation efficiency analysis

The photocatalytic properties of materials and their application in implementing enhanced wastewater treatment procedures on an industrial scale also affect their electrical performances. For these reasons, the materials used in such applications must be obtained from cheap and abundant resources, and their production methods must be simple. In addition, optimizing material properties, such as conductivity, dopant ratio, particle size, etc., causes a difference in electrical, optical, and morphological properties and photocatalytic abilities [75, 81]. Thus, the properties of the synthesized materials can be exploited to achieve the desired properties.

The decolorization of methylene blue (Methylthioninium chloride, MB) as a dye has been comprehensively used in industrial implementations, and testing on this provides good information on the effectiveness of the catalyst. In addition, nanostructured metal oxide materials are a good source of electrons for redox reactions; they are usually cheap and easy to produce and do not require any expensive chemical materials to supplement.

In this study, we synthesized ZnO NRs/CuO NC and Sr-doped ZnO NRs/CuO NCs at different Sr concentrations. The presence of CuO in the ZnO-based composite contributes to improved photocatalytic activity by enhancing charge separation and reducing recombination. Previous studies also demonstrated that multi-component oxide composites (e.g., ZnO–CuO–CdO) exhibit higher degradation efficiency and kinetic rate constants than individual oxides. The photocatalytic decolorization of MB with manufactured ZnO NRs/CuO NC and Sr-doped ZnO/CuO NC was measured by UV–vis spectra and observed that the main absorption peak at 665 nm systematically decreased with UV light exposure and became almost transparent after 120 min under UV light irradiation. The measured absorbance results are presented in Fig. 10. The decreasing trend observed in the absorbance values of all samples indicates the efficiency of the photocatalytic decolorization process for ZnO NRs/CuO NC and Sr-doped ZnO/CuO NC. Although they are prepared under identical conditions, the samples' behavior may differ due to the amount of dopant after the catalyst sample is added until adsorption-desorption equilibrium is achieved. Therefore, these initial conditions differ for doped and un-doped ZnO NR/CuO NC. However, the degradation efficiency and first-order kinetic plots of ZnO NRs/CuO NC, ZnO NRs/CuO: Sr (2.0 %), and ZnO NRs/CuO:Sr (4.0 %) more clearly reveal the effect of doping on the decolorization process.

The degradation process can be summarized as follows: ZnO and CuO have relatively low bandgap energy values and UV light easily excites an electron from the valence band to the conduction band, creating a hole in the valence band (Fig. 11.).

The excited electrons participate in the formation of superoxide and

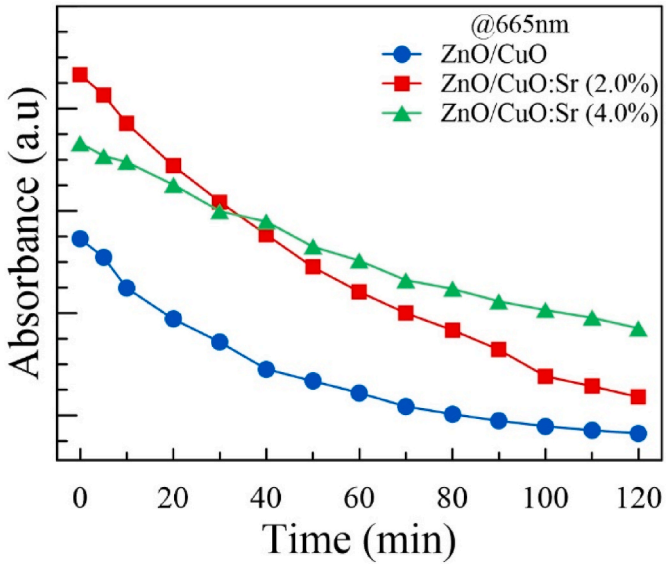

Fig. 10. Changes in the absorbance values of MB solutions with the UV light exposure time of the ZnO NRs/CuO NC and the Sr-doped ZnO NRs/CuO NC.

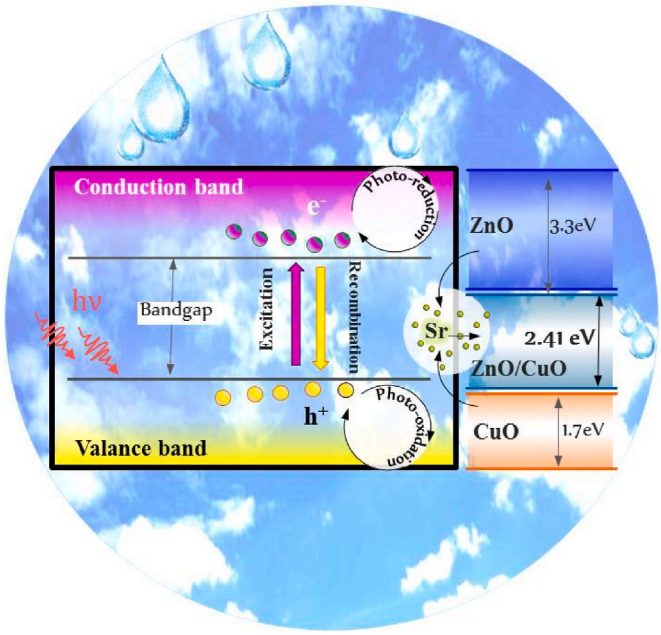

Fig. 11. Degradation of Sr-doped ZnO NRs/CuO NC.

hydroxyl radicals, which subsequently oxidize the MB molecules. The degradation of MB under UV irradiation proceeds through the following four-step mechanism [75,84–86].

i. Photoexcitation of ZnO/CuO and creation of electron (e^-)/hole (h^+) pairs via UV light:

$$CuO–ZnO + h\nu \rightarrow CuO–ZnO + (e^- + h^+)$$

ii. Oxygen absorption of ZnO/CuO:

$$CuO–ZnO\ (e^-) + O_2 \rightarrow CuO–ZnO + \bullet O_2^-$$

iii. Ionization of water:

$$H_2O \rightarrow H^+ + OH,$$

$$\bullet O_2^- + 2H^+ + e^- \rightarrow H_2O_2 \rightarrow 2\ \bullet OH$$

iv. Protonation of the excited ZnO NRs/CuO NC:

$$\bullet OH + MB \rightarrow \text{Degraded products}$$

$$\bullet O_2^- + MB \rightarrow \text{Degraded products}$$

The degradation efficiency (η) was calculated using the following relation [85,86]:

$$\eta = \left(C_0 - C_t/C_0\right) x100\% \quad (5)$$

Where C_0 is the initial concentration, and C_t is the concentration (mg/l) after irradiation at 10-min intervals. As shown in Fig. 12, the degradation efficiency of the ZnO NRs/CuO NC and Sr-doped ZnO NRs/CuO NC gradually decreased, reaching a value below 50 % after 120 min. In addition, all the results indicate that the degradation kinetics were in a first-order process (Fig. 13(a).

The degradation rate constant (k) was obtained from linear fits to first-order kinetic plots (Fig. 13(b). The degradation rates of the ZnO NRs/CuO NC and 2.0 % Sr-doped ZnO NRs/CuO NC were very similar, and increasing Sr doping slightly decreased this rate. This phenomenon can be explained by excess Sr doping, which reduces both the formation of e^-/h^+ pairs and the effectiveness of ZnO NRs/CuO, the main component of degradation, in steps (i) and (ii) of the degradation process, as mentioned above.

In photocatalytic degradation, some metrics help to assess the catalyst's ability to drive the reaction, especially within heterogeneous reaction environments. The terms "active site," "turn-over number (TON)," and "turn-over frequency (TOF)" are fundamental for assessing and quantifying catalyst efficiency in heterogeneous catalysis. Active sites are called specific regions on the catalyst surface where reactant molecules adsorb, and catalytic reactions are facilitated. The nature and characteristics of these active sites significantly influence the efficiency and selectivity of the catalytic process. TON provides a quantitative measure of a catalyst's efficiency by dividing the total number of product molecules by the number of available active sites or catalyst molecules in the system [81,87–89];

$$\text{TON} = \frac{(\%\eta)(\text{Number of molecules of substrate})}{\text{Number of molecules of catalyst}} \quad (6)$$

The TOF offers a dynamic evaluation of catalytic performance, representing the number of reaction cycles occurring over a set time period

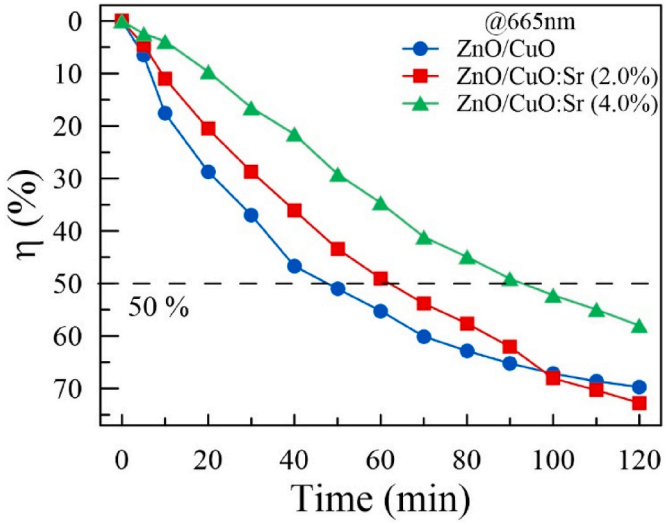

Fig. 12. Changes in the degradation efficiency of MB solutions upon UV light exposure of ZnO NRs/CuO NCs and Sr-doped ZnO NRs/CuO NC.

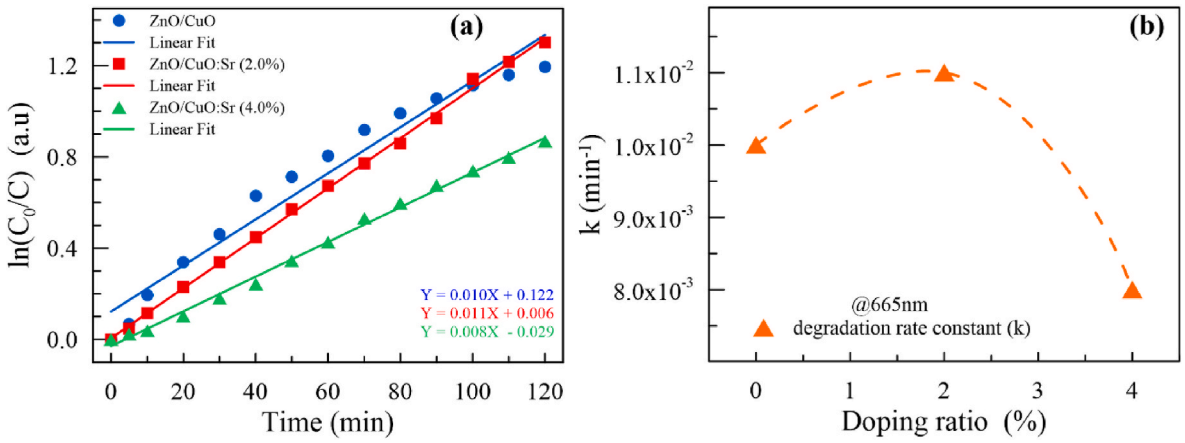

Fig. 13. First-order kinetic plots of ZnO NRs/CuO NC (●), ZnO NRs/CuO:Sr (2.0 %) (■) and ZnO NRs/CuO:Sr (4.0 %) (▲) NC (**a**) and changes in the degradation rate constants (k) with increasing Sr doping percentage (**b**).

and expressed as [81,88];

$$\mathrm{TOF} = \frac{\mathrm{TON}}{\mathrm{time}} \tag{7}$$

The TOF emphasizes the catalyst activity over time, which is especially useful when evaluating ongoing reactions.

In our experiment, 30 mg ZnO NRs/CuO NC contained 36 % CuO, and the active site number was calculated as 37.14 mmol. Similarly, a 30 ml 10 ppm MB solution contained 9.379×10^{-7} mol, representing the number of catalyst molecules used as catalyst number. The active sites of the doped atoms were also calculated, considering the doping level, as given in Table 3.

The calculated results show an increase in TON and TOF as the doping concentration increases with 2.0 % Sr doping, suggesting that ZnO nanoparticles exhibit slightly boosted catalytic efficiency. However, when the Sr doping rate was 4.0 %, the degradation efficiency decreased significantly, and accordingly, the TON and TOF values decreased (although the total active site is almost constant). The results obtained here are essential in revealing the effect of doping on the mechanisms of the photocatalytic degradation process. While the impact of excess doping ions on the degradation parameters is positive for low doping rates, the presence of positive ions prevents the formation of e^-/h^+ pairs when doping increases.

The photocatalytic performance of composite materials is not solely determined by the material itself but also by factors such as synthesis method, surface area, crystallinity, and the nature of the pollutant. Compared to systems like ZnO/TiO_2, ZnO nanorods/CuO nanocomposites offer certain advantages, mainly due to CuO's narrower bandgap, which facilitates more effective charge separation during degradation reactions [90,91]. Although TiO_2 is known for its photostability under UV light, this property can sometimes be a limitation in photocatalytic systems [92]. While ZnO/CuO heterostructures have demonstrated higher photocatalytic activity than pure ZnO or CuO in the literature (with reported kinetic rate constants as high as 0.042–0.052 min^{-1} for methylene blue degradation under UV light [93–95] the lower rate constant obtained in this study (0.010 min^{-1}) may be attributed to factors such as suboptimal CuO content, larger particle size, or reduced light intensity. Nevertheless, the results confirm that the ZnO/CuO composite still performs better than its individual components and holds potential for further enhancement.

Table 3
Calculated parameters for the photocatalytic degradation of ZnO NRs/CuO NC and Sr-doped ZnO NRs/CuO NCs.

Sr Doping (%)	Active site subs. ($x10^{-4}$ mol)	Active site dopant ($x10^{-6}$ mol)	Total active site ($x10^{-3}$ mol)	%η	TON	TOF ($x10^{-3}$ min^{-1})
0.0	0	0	37.14	69.72	0.176	1.47
2.0	6.0	6.9	37.08	72.75	0.184	1.53
4.0	12.0	13.7	37.03	58.02	0.147	1.22

* The number of molecules of MB is 9.379×10^{-7} mol, and the time was 120 min.

4. Conclusions

In conclusion, this study comprehensively analyzes the effects of Sr^{2+} doping on the structural, surface, and functional properties. Evaluations using various techniques revealed that Sr^{2+} doping significantly transformed the material's properties. SEM analysis showed that Sr^{2+} doping markedly changed the film's surface morphology and promoted the formation of larger, irregular particle clusters. EDX analyses confirmed that the Sr dopant was homogeneously dispersed in the ZnO/CuO matrix and was successfully integrated without phase separation. AFM measurements showed an increase in RMS roughness values from 91.42 nm to 127.56 nm and 143.82 nm, indicating that Sr doping optimized the surface properties of the composite structure. With the increase in Sr^{2+} doping, a decrease in the crystal size from 36.20 to 29.90 nm was observed. This shrinkage indicates that Sr^{2+} ions disrupt crystal growth and introduce defects into the structure. Calculated quantifying catalyst efficiency numbers (TON and TOF) show both increases as the doping concentration increases with 2.0 % Sr doping, indicating enhanced catalytic efficiency. This study demonstrates that Sr^{2+} doping effectively alters the surface morphology, crystalline structure, and functional properties of ZnO/CuO nanocomposite films. The enhanced surface area, improved electrical properties, and improved photocatalytic efficiency of the Sr-doped ZnO/CuO films indicate their potential for use in environmental remediation and optoelectronic devices.

CRediT authorship contribution statement

Ali Tekin: Writing – review & editing, Data curation. **Raşit Aydın:** Writing – review & editing, Supervision, Methodology, Investigation, Formal analysis, Data curation. **Ümmühan Akın:** Writing – review & editing, Investigation, Data curation. **Osman Kahveci:** Writing – review & editing, Investigation, Data curation. **Abdullah Akkaya:** Writing – review & editing, Investigation, Data curation. **Hüsnü Kara:** Data curation, Formal analysis. **Bünyamin Şahin:** Supervision, Methodology, Investigation, Data curation.

Declaration of competing interest

The authors declare that they have no known competing financial interests or personal relationships that could have appeared to influence the work reported in this paper.

Acknowledgments

This work was supported by The Scientific and Technological Research Council of Türkiye (TUBITAK) 2209-A - Research Project Support Programme for Undergraduate Students (Application/Project No: 1919B012322851).

Data availability

Data will be made available on request.

References

[1] M. Hashim, M. Usman, S. Ahmad, R. Shah, A. Ali, N.U. Rahman, ZnO/NiO nanocomposite with enhanced photocatalytic H2 production, Int. J. Photoenergy 2024 (2024) 2676368.
[2] M. Ananthkumar, J. Jayaprakash, A. Debnath, M.F. Albeshr, R. Mythili, P. Akilan, A. Kannan, S. Vignesh, V. Chandrasekaran, Physicochemical and photocatalytic properties of Ag2CrO4/Fe2O3/CeO2 ternary nanocomposite, Luminescence 39 (2024) e4840.
[3] F.A. Alharthi, A.S. Ababtain, H.S. Alanazi, W.S. Al-Nafaei, I. Hasan, Synthesis of Zn3V2O8/rGO nanocomposite for photocatalytic hydrogen production, Inorganics 11 (3) (2023) 93.
[4] Z. Azmoodeh, S. Nasirian, H. Milani Moghaddam, Improving H2 gas sensing with ZnMn2O4/Polypyrrole Nanocomposite, Int. J. Hydrogen Energy 85 (2024) 854–864.
[5] A.M. Omar, M.H. Hassan, E. Daskalakis, A. Smith, J. Donoghue, W. Mirihanage, P. J.D.S. Bartolo, Biomimetic dual sensing polymer nanocomposite for biomedical applications, Front. Bioeng. Biotechnol. 12 (2024).
[6] Q. Cao, W. Zhu, W. Chen, X. Chen, R. Yang, S. Yang, H. Zhang, X. Gui, J. Chen, Nonsolid TiOx nanoparticles/PVDF nanocomposite for improved energy storage performance, ACS Appl. Mater. Interfaces 14 (2022) 8226–8234.
[7] B. Lei, H. Zhang, Q. Zhao, W. Liu, Y. Wei, Y. Lu, T. Xiao, J. Kong, W. Cai, Facile synthesis of ZnO/WO3 nanocomposite porous films for high-performance gas sensing of multiple VOCs, Nanomaterials 13 (4) (2023) 733.
[8] A.Y. Alhato, R. Kumar, M.A. Barakat, Integrated ozonation Ni-NiO/Carbon/g-C3N4 nanocomposite-mediated catalytic decomposition of organic contaminants in wastewater under visible light, Nanomaterials 14 (2) (2024) 190.
[9] F. Islam, S. Shohag, M.J. Uddin, M.R. Islam, M.H. Nafady, A. Akter, S. Mitra, A. Roy, T.B. Emran, S. Cavalu, Exploring the journey of zinc oxide nanoparticles (ZnO-NPs) toward biomedical applications, Materials 15 (6) (2022) 2160.
[10] M. Ashaduzzaman, D. Saha, O. Saha, M.M. Rahaman, N. Mustary, Interfacially self-assembled Fe2O3 nanoparticles decorated kaolinite for high performance anti-bacterial and anti-cancerous agents, Inorganic Nano-Metal Chem., 1-12.
[11] D.R. Rout, S. Chaurasia, H.M. Jena, Enhanced photocatalytic degradation of malachite green using manganese oxide doped graphene oxide/zinc oxide (GO-ZnO/Mn2O3) ternary composite under sunlight irradiation, J. Environ. Manag. 318 (2022) 115449.
[12] M. Khandelwal, K. Soni, K.P. Misra, A. Bagaria, D.S. Rathore, G. Pemawat, R. Singh, R.K. Khangarot, Facile fabrication of a novel chitosan/carboxymethyl cellulose/bentonite/CuO nanocomposite for enhanced photocatalytic and antibacterial applications, RSC Adv. 15 (2025) 3365–3377, https://doi.org/10.1039/d4ra08437c. Electronic supplementary information (ESI) available. See.
[13] G.G. Welegergs, H.G. Gebretinsae, M.G. Tsegay, C. Mtshali, N. Mongwaketsia, K. Cloete, Z.Y. Nuru, S. Dube, M. Maaza, Single-layered biosynthesized copper oxide (CuO) nanocoatings as solar-selective absorber, Appl. Sci. 13 (3) (2023) 1867.
[14] A. Jabeen, A. Khan, P. Ahmad, A. Khalid, Z. Majeed, Z. Anjum, Y. Modafer, O. A. Jefri, A.M. Alanazi, A.M. Saeedi, A.H. Alsehli, M.M. Alsowayigh, M. U. Khandaker, I. Boukhris, Biomedical and photocatalytic dye degradation studies of Cymbopogon citratus mediated copper oxide nanoparticles (CuO NPs), J. Drug Deliv. Sci. Technol. 87 (2023) 104795.
[15] B. Şahin, T. Kaya, A first-principle study of nanostructured CuO thin film-based caffeine sensing scheme, Sensor Actuator Phys. 332 (2021) 113138.
[16] E.E. Elemike, D.C. Onwudiwe, M. Singh, Eco-friendly synthesis of copper oxide, zinc oxide and copper oxide–zinc oxide nanocomposites, and their anticancer applications, J. Inorg. Organomet. Polym. Mater. 30 (2020) 400–409.
[17] M. Gerawork, Photodegradation of methyl orange dye by using Zinc Oxide – copper Oxide nanocomposite, Optik 216 (2020) 164864.
[18] A.A. Alswat, M.B. Ahmad, T.A. Saleh, Preparation and characterization of Zeolite \Zinc oxide-copper oxide nanocomposite: antibacterial activities, Collo. Interface Sci. Commun. 16 (2017) 19–24.
[19] L. Cao, J. Kiely, M. Piano, R. Luxton, A copper oxide/zinc oxide composite nano-surface for use in a biosensor, Materials 12 (7) (2019) 1126.
[20] S.M. Yakout, A.M. El-Sayed, Enhanced ferromagnetic and photocatalytic properties in Mn or Fe doped p-CuO/n-ZnO nanocomposites, Adv. Powder Technol. 30 (2019) 2841–2850.
[21] H. Safdar, R. Aydın, B. Şahin, Syntheses, structural evolution, electrical and optoelectronic characterization of ZnO/CuO composite films doped with transition metal Mn^{2+} ions, Ceram. Int. 48 (2022) 26678–26688.
[22] X. Jia, H. Zhang, B. Ren, J. Xie, P. Ge, B. Zhang, Fe–Ni–Ce–Zr-modified CuO–ZnO catalyst for methanol steam reforming, J. Energy Inst. 110 (2023) 101316.
[23] I. Mansouri, F. Saib, S. Boulahlib, A. Laachachi, M. Özacar, Y. Bessekhouad, Effect of Sr-doping toward the optoelectrical ZnO properties, Inorg. Chem. Commun. 162 (2024) 112236.
[24] C. You, Z. Li, S. Zhang, G. Jiang, H. Zhang, Electrical properties of Sr-modified CuO ceramics, J. Mater. Sci. Mater. Electron. 32 (2021) 15907–15916.
[25] D.H. Ramakrishnegowda, K.S. Chandrakantha, D. Urs, M. Elfeky, J. Krishnegowda, S. Rangappa, K.S. Rangappa, S. Shivanna, Synthesis of p-CuO/n-ZnO heterostructure by microwave hydrothermal method and evaluation of its photo and bio-catalytic performance, Heliyon 9 (2023) e22758.
[26] R. Kumar, K. Kumar, S. Sharma, N. Thakur, N. Thakur, Multifunctional properties of microwave assisted CuO/Cu2O-ZnO mixed metal oxide nanocomposites, J. Mater. Sci. Mater. Electron. 34 (2023) 1255.
[27] X. Wang, H.J. Cho, p-CuO nanowire/n-ZnO nanosheet heterojunction-based near-UV sensor fabricated by electroplating and thermal oxidation process, Mater. Lett. 223 (2018) 170–173.
[28] M.A. Subhan, N. Uddin, P. Sarker, A.K. Azad, K. Begum, Photoluminescence, photocatalytic and antibacterial activities of CeO2·CuO·ZnO nanocomposite fabricated by co-precipitation method, Spectrochim. Acta Mol. Biomol. Spectrosc. 149 (2015) 839–850.
[29] B. Şahin, R. Aydin, H. Cetin, Tuning the morphological, structural, optical and dielectric properties of hausmannite (Mn3O4) films by doping heavy metal lead, Superlattice. Microst. 143 (2020) 106546.
[30] A.F. Abdulrahman, N.M. Abd-Alghafour, S.M. Ahmed, Optimization and characterization of SILAR synthesized ZnO nanorods for UV photodetector sensor, Sensor Actuator Phys. 323 (2021) 112656.
[31] T. Jamil, S. Yasin, N. Ramzan, Z. Aslam, A. Ikhlaq, U.Y. Qazi, R. Javaid, Treatment of textile wastewater by a novel clay/TiO2/ZnO-based catalyst, applying a synergic catalytic ozonation–electroflocculation process, Catalysts 13 (9) (2023) 1315.
[32] M. Marzec, A. Listosz, A. Malik, M. Kulik, K. Jóźwiakowski, Organic pollutants removal in a hybrid constructed wetland wastewater treatment plant with an aeration system, Water 16 (7) (2024) 947.
[33] M. Chang, T. Zhu, T. Xiao, J. Wang, N. Wang, Y. Song, Y. Wang, Novel process for organic wastewater treatment using aerobic composting technology: shifting from pollutant removal towards resource recovery, Sci. Total Environ. 913 (2024) 169522.
[34] Y. Shi, X. Chen, Q. Wu, H. Zhen, S. Wang, H. Dong, J. Wang, Y. Li, Enhance organic pollutants removal of wastewater by a PVDF/PDA-TiO2 composite membrane with photocatalytic property, J. Environ. Chem. Eng. 11 (2023) 110389.
[35] D. Dhinasekaran, P. Soundharraj, M. Jagannathan, A.R. Rajendran, S. Rajendran, Hybrid ZnO nanostructures modified graphite electrode as an efficient urea sensor for environmental pollution monitoring, Chemosphere 296 (2022) 133918.
[36] R. Yadav, T.S. Chundawat, P.K. Surolia, D. Vaya, Photocatalytic degradation of textile dyes using β-CD-CuO/ZnO nanocomposite, J. Phys. Chem. Solid. 165 (2022) 110691.
[37] S. Ullah, S. Aqsa Batool Bukhari, H. Nasir, T. Akhtar, S. Mahboob, M. Zahid, Efficient photocatalytic degradation of profenofos by CuO-ZnO nanocomposite, J. Photochem. Photobiol. Chem. 455 (2024) 115787.
[38] V. Kumari, S. Yadav, J. Jindal, S. Sharma, K. Kumari, N. Kumar, Synthesis and characterization of heterogeneous ZnO/CuO hierarchical nanostructures for photocatalytic degradation of organic pollutant, Adv. Powder Technol. 31 (2020) 2658–2668.
[39] L. Xu, Y. Zhou, Z. Wu, G. Zheng, J. He, Y. Zhou, Improved photocatalytic activity of nanocrystalline ZnO by coupling with CuO, J. Phys. Chem. Solid. 106 (2017) 29–36.
[40] H. Satılmış, M. Acar, R. Aydın, A. Akkaya, O. Kahveci, B. Şahin, E. Ayyıldız, Cd-supported CuO-ZnO binary oxide thin films: synthesis, microstructural, and optoelectronic properties, Opt. Mater. 148 (2024) 114851.
[41] H. Bishwakarma, A. Kumar Das, P. Kumar, P. Kumar Singh, M.M. Awad, Structure and electrochemical properties of CuO-ZnO nanocomposite produced by the one-step novel discharge process, J. Taibah Univ. Sci. 17 (2023) 2188017.
[42] H. Shaili, E. Salmani, M. Beraich, A. Elhat, M. Rouchdi, M. Taibi, H. Ez-Zahraouy, N. Hassanain, A. Mzerd, Revealing the impact of strontium doping on the optical, electronic and electrical properties of nanostructured 2H-CuFeO 2 delafossite thin films, RSC Adv. 11 (2021) 25686–25694.
[43] A. Srivastava, N. Kumar, K.P. Misra, S. Khare, Enhancement of band gap of ZnO nanocrystalline films at a faster rate using Sr dopant, Electron. Mater. Lett. 10 (2014) 703–711.
[44] R. Savari, J. Rouhi, O. Fakhar, S. Kakooei, D. Pourzadeh, O. Jahanbakhsh, S. Shojaei, Development of photo-anodes based on strontium doped zinc oxide-reduced graphene oxide nanocomposites for improving performance of dye-sensitized solar cells, Ceram. Int. 47 (2021) 31927–31939.
[45] C. Shetty, V. Veena Devi Shastrimath, R. Bairy, Tuning the structural, morphological and optical properties of Sr-doped BFO thin films, Phase Transitions 95 (2022) 202–211.
[46] X. Zhang, Y. Huang, B. Wang, X. Chang, H. Yang, J. Lan, S. Wang, H. Qiao, H. Lin, S. Han, Y. Guo, X. Zhang, A functionalized Sm/Sr doped TiO2 nanotube array on titanium implant enables exceptional bone-implant integration and also self-antibacterial activity, Ceram. Int. 46 (2020) 14796–14807.

[47] A. Ouhaibi, M. Ghamnia, M.A. Dahamni, V. Heresanu, C. Fauquet, D. Tonneau, The effect of strontium doping on structural and morphological properties of ZnO nanofilms synthesized by ultrasonic spray pyrolysis method, J. Sci. Adv. Mater. Devices 3 (2018) 29–36.
[48] R. Aydin, O. Kahveci, A. Akkaya, B. Şahin, E. Ayyıldız, Conductometric flexible CuO-based sweat-loss monitoring sensor for future wearable technology in healthcare, ACS Omega 8 (2023) 42576–42585.
[49] B.R. Khanam, M.G. Kotresh, U.V. Khadke, Enhanced crystallographic and physicochemical properties of chromium-embedded ZnO nanoparticles, Chem. Phys. Impact 8 (2024) 100518.
[50] W.H. Alsaedi, W.S. Mohamed, H.A. Qasem, M. Alahmadi, A.H. Alsulami, Y. M. Asiri, K. Al-Ghamdi, A.M. Abu-Dief, Fabrication of CuO/PdO nanocomposites for biomedical applications, Inorg. Chem. Commun. 170 (2024) 113166.
[51] M.H. Kabir, A. Bhattacharjee, M.M. Islam, M.S. Rahman, M.S. Rahman, M.K. R. Khan, Effect of Sr doping on structural, morphological, optical and electrical properties of spray pyrolized CdO thin films, J. Mater. Sci. Mater. Electron. 32 (2021) 3834–3842.
[52] M. Ikram, A. Shahzadi, M. Bilal, A. Haider, A. Ul-Hamid, W. Nabgan, J. Haider, S. Ali, F. Medina, M. Imran, Strontium-doped chromium oxide for RhB reduction and antibacterial activity with evidence of molecular docking analysis, Front. Chem. 11 (2023).
[53] R.R. Chandrapal, S. Bharathkumar, G. Bakiyaraj, V. Ganesh, J. Archana, M. Navaneethan, Hydrothermally synthesized strontium-modified ZnO hierarchical nanostructured photocatalyst for second-generation fluoroquinolone degradation, Appl. Nanosci. 12 (2022) 1869–1884.
[54] A. Pandey, P. Yadav, A. Fahad, P. Kumar, M.K. Singh, Enhancing structural, optical and dielectric properties of CuO–ZnO nanocomposites through controlled CuO and ZnO concentration adjustments, Bull. Mater. Sci. 47 (2024) 141.
[55] A.K. Rajan, L. Cindrella, Ameliorating the photovoltaic conversion efficiency of ZnO nanorod based dye-sensitized solar cells by strontium doping, Superlattice. Microst. 128 (2019) 14–22.
[56] H.A. Abo-Mosallam, E.A. Mahdy, Effect of strontium on crystallization characteristics and properties of ZnO-Fe2O3-B2O3-P2O5 glass-ceramics for biomedical applications, J. Non-Cryst. Solids 583 (2022) 121467.
[57] K. Ravichandran, N.S. Jyothi, R. Rathi, N. Dineshbabu, R. Shalini, A. Viji, K. Neethidevan, Intermediate electron trap levels generation and enhanced carrier concentration in ZnO by strontium and molybdenum co-doping: an effective approach for dye degradation, J. Mater. Sci. Mater. Electron. 34 (2023) 5.
[58] S.A. Khan, F. Noreen, S. Kanwal, A. Iqbal, G. Hussain, Green synthesis of ZnO and Cu-doped ZnO nanoparticles from leaf extracts of Abutilon indicum, Clerodendrum infortunatum, Clerodendrum inerme and investigation of their biological and photocatalytic activities, Mater. Sci. Eng. C 82 (2018) 46–59.
[59] A. Akkaya, B. Şahin, R. Aydın, H. Çetin, E. Ayyıldız, Solution-processed nanostructured ZnO/CuO composite films and improvement its physical properties by lustrous transition metal silver doping, J. Mater. Sci. Mater. Electron. 31 (2020) 14400–14410.
[60] N. Rao, M. Rao, Structural and optical investigation of ZnO nanopowders synthesized from zinc chloride and zinc nitrate, Am. J. Mater. Sci. 5 (2015) 66–68.
[61] A. Akkaya, O. Kahveci, R. Aydın, B. Şahin, Amplifying main physical characteristics of CuO films using ascorbic acid as the reducer and stabilizer agent, Appl. Phys. A 127 (2021) 911.
[62] R. Saravanan, S. Karthikeyan, V.K. Gupta, G. Sekaran, V. Narayanan, A. Stephen, Enhanced photocatalytic activity of ZnO/CuO nanocomposite for the degradation of textile dye on visible light illumination, Mater. Sci. Eng. C 33 (2013) 91–98.
[63] E. Abbasi, M. Haghighi, R. Shokrani, M. Shabani, Copper plasmon-induced Cu-doped ZnO-CuO double-nanoheterojunction: in-situ combustion synthesis and photo-decontamination of textile effluents, Mater. Res. Bull. 129 (2020) 110880.
[64] M. Mansournia, L. Ghaderi, CuO@ZnO core-shell nanocomposites: novel hydrothermal synthesis and enhancement in photocatalytic property, J. Alloys Compd. 691 (2017) 171–177.
[65] S. Das, V.C. Srivastava, Synthesis and characterization of ZnO/CuO nanocomposite by electrochemical method, Mater. Sci. Semicond. Process. 57 (2017) 173–177.
[66] A.A. Sakib, S.M. Masum, J. Hoinkis, R. Islam, M.A. Molla, Synthesis of CuO/ZnO nanocomposites and their application in photodegradation of toxic textile dye, J. Compos. Sci. 3 (3) (2019) 91.
[67] B. Şahin, R. Aydın, H. Çetin, Variation of the key morphological, structural, optical and electrical properties of SILAR CdO with alkaline earth Ca2+ ions doping, Ceram. Int. 45 (2019) 16748–16758.
[68] K. Radhi Devi, G. Selvan, M. Karunakaran, I.L. Poul Raj, V. Ganesh, S. AlFaify, Enhanced room temperature ammonia gas sensing properties of strontium doped ZnO thin films by cost-effective SILAR method, Mater. Sci. Semicond. Process. 119 (2020) 105117.
[69] I.S. Karthigayan, D. Gopinath, P.B. Shalini, L.B. Chandrasekar, S.R. Ahamed, Structural, optical and electrochemical properties of Sr-doped ZnO nanoparticles, Solid State Sci. 155 (2024) 107651.
[70] Y.S. Tamgadge, S.S. Talwatkar, A.L. Sunatkari, V.G. Pahurkar, G.G. Muley, Studies on nonlocal optical nonlinearity of Sr–CuO–polyvinyl alcohol nanocomposite thin films, Thin Solid Films 595 (2015) 48–55.
[71] A. Kumawat, S. Chattopadhyay, K.P. Misra, N. Halder, S.K. Jain, B.L. Choudhary, Blue-shift in the optical band gap of sol-gel derived Zn(1-x)SrxO nanoparticles, Solid State Sci. 108 (2020) 106379.
[72] S.N. V, B. Angadi, M.H. M, S. C, R. M, Investigation of Sr doping on structural, morphological, optical, photocatalytic and antifungal properties of NiO thin films prepared by spray coating technique, Curr. Appl. Phys. 72 (2025) 39–50.
[73] M.S. Nadeem, M. Baoji, M.M. Alam, N.N. Riaz, A.G. Al-Sehemi, T. Munawar, F. Mukhtar, A.W. Rabbani, A. Naz, M.A. Al-Tahan, F. Iqbal, Sr-doped ZnO thin film on a silicon substrate (100) grown by sol-gel method: structural and optical study, Opt. Mater. 157 (2024) 116106.
[74] Z.-Y. Zhang, T.-Y. Huang, D.-J. Zhai, H.-B. Wang, K.-Q. Feng, L. Xiang, Study on strontium doped bioactive coatings on titanium alloys surfaces by micro-arc oxidation, Surf. Coating. Technol. 451 (2022) 129045.
[75] O. Kahveci, A. Akkaya, E.K. Sarıkaya, M. Çanlı, R. Aydın, B. Şahin, E. Ayyıldız, Construction of unary and ternary ZnO–CuO–CdO composite thin films and comprehensive analysis of their optical, electrical, and photocatalytic performance, J. Alloys Compd. 997 (2024) 174827.
[76] D. Ramírez-Ortega, A.M. Meléndez, P. Acevedo-Peña, I. González, R. Arroyo, Semiconducting properties of ZnO/TiO2 composites by electrochemical measurements and their relationship with photocatalytic activity, Electrochim. Acta 140 (2014) 541–549.
[77] N.A. Vorobyeva, M.N. Rumyantseva, R.B. Vasiliev, V.F. Kozlovskiy, Y. M. Soshnikova, D.G. Filatova, V.B. Zaytsev, A.V. Zaytseva, A.M. Gaskov, Doping effects on electrical and optical properties of spin-coated ZnO thin films, Vacuum 114 (2015) 198–204.
[78] O. Kahveci, Preparation of 3-D porous pure Al electrode for Al-air battery anode and comparison of its electrochemical performance with a smooth surface electrode, Chemelectrochem 10 (2023) e202300221.
[79] A. Akkaya, E. Ayyıldız, Automation software for semiconductor research laboratories: electrical parameter calculation program (SeCLaS-PC), J. Circ. Syst. Comput. 29 (2020) 2050215.
[80] S. Soğan, E. Yücel, E.K. Sarıkaya, O. Kahveci, R. Aydın, A. Akkaya, B. Şahin, Growth and characterization of Fe-doped CuO/ZnO binary oxide thin films for possible optoelectronic applications, Opt. Mater. 152 (2024) 115557.
[81] A. Akkaya, E.K. Sarıkaya, O. Kahveci, R. Aydın, B. Şahin, E. Ayyıldız, Hyaluronic acid mediated ZnO-NPs: in relation to electrical and photocatalytic activity for dye degradation, J. Alloys Compd. 1005 (2024) 175861.
[82] T.A. Vijayan, R. Chandramohan, S. Valanarasu, J. Thirumalai, S.P. Subramanian, Comparative investigation on nanocrystal structure, optical, and electrical properties of ZnO and Sr-doped ZnO thin films using chemical bath deposition method, J. Mater. Sci. 43 (2008) 1776–1782.
[83] K. Ellmer, Resistivity of polycrystalline zinc oxide films: current status and physical limit, J. Phys. Appl. Phys. 34 (2001) 3097.
[84] B. Dong, X. Yu, Z. Dong, X. Yang, Y. Wu, Facile synthesis of ZnO nanoparticles for the photocatalytic degradation of methylene blue, J. Sol. Gel Sci. Technol. 82 (2017) 167–176.
[85] T. Munawar, F. Iqbal, S. Yasmeen, K. Mahmood, A. Hussain, Multi metal oxide NiO-CdO-ZnO nanocomposite–synthesis, structural, optical, electrical properties and enhanced sunlight driven photocatalytic activity, Ceram. Int. 46 (2020) 2421–2437.
[86] S. Harish, J. Archana, M. Sabarinathan, M. Navaneethan, K.D. Nisha, S. Ponnusamy, C. Muthamizhchelvan, H. Ikeda, D.K. Aswal, Y. Hayakawa, Controlled structural and compositional characteristic of visible light active ZnO/CuO photocatalyst for the degradation of organic pollutant, Appl. Surf. Sci. 418 (2017) 103–112.
[87] S. Kozuch, J.M.L. Martin, "Turning over" definitions in catalytic cycles, ACS Catal. 2 (2012) 2787–2794.
[88] L. Gomathi Devi, R. Shyamala, Photocatalytic activity of SnO2–α-Fe_2O_3 composite mixtures: exploration of number of active sites, turnover number and turnover frequency, Mater. Chem. Front. 2 (2018) 796–806.
[89] C.-L. Chiang, K.-S. Lin, H.-W. Chuang, Direct synthesis of formic acid via CO_2 hydrogenation over Cu/ZnO/Al_2O_3 catalyst, J. Clean. Prod. 172 (2018) 1957–1977.
[90] A. Muzakki, H. Shabrany, R. Saleh, Synthesis of ZnO/CuO and TiO2/CuO Nanocomposites for Light and Ultrasound Assisted Degradation of a Textile Dye in Aqueous Solution, 2016.
[91] A.B. Migdadi, M.K. Alqadi, F.Y. Alzoubi, H.M. Al-Khateeb, W.T. Bani-Hani, Photocatalytic activity of prepared ZnO/CuO nanocomposites and kinetic degradation study of methylene blue, J. Mater. Sci. Mater. Electron. 33 (2022) 26744–26763.
[92] E. Widyastuti, C.-T. Chiu, J.-L. Hsu, Y. Chieh Lee, Photocatalytic antimicrobial and photostability studies of TiO_2/ZnO thin films, Arab. J. Chem. 16 (2023) 105010.
[93] A.R. Bhapkar, S. Bhame, A review on ZnO and its modifications for photocatalytic degradation of prominent textile effluents: synthesis, mechanisms, and future directions, J. Environ. Chem. Eng. 12 (2024) 112553.
[94] R.S. Shinde, S.D. Khairnar, M.R. Patil, V.A. Adole, P.B. Koli, V.V. Deshmane, D. K. Halwar, R.A. Shinde, T.B. Pawar, B.S. Jagdale, A.V. Patil, Synthesis and characterization of ZnO/CuO nanocomposites as an effective photocatalyst and gas sensor for environmental remediation, J. Inorg. Organomet. Polym. Mater. 32 (2022) 1045–1066.
[95] A.G. Acedo-Mendoza, A. Infantes-Molina, D. Vargas-Hernández, C.A. Chávez-Sánchez, E. Rodríguez-Castellón, J.C. Tánori-Córdova, Photodegradation of methylene blue and methyl orange with CuO supported on ZnO photocatalysts: the effect of copper loading and reaction temperature, Mater. Sci. Semicond. Process. 119 (2020) 105257.